Environmental Science and Pollution Research (2023) 30:87185–87198
https://doi.org/10.1007/s11356-023-28685-5

RESEARCH ARTICLE

Removal of tetracycline in aqueous solution by iron-loaded biochar derived from polymeric ferric sulfate and bagasse

Qiaojing Liu[1] · Xingfeng Cao[1] · Tiantian Yue[1] · Fengzhi Zhang[1] · Shaoyuan Bai[1,2,3] · Liheng Liu[1,2,3]

Received: 14 March 2023 / Accepted: 4 July 2023 / Published online: 7 July 2023
© The Author(s), under exclusive licence to Springer-Verlag GmbH Germany, part of Springer Nature 2023

Abstract

In this study, the tetracycline (TC) removal performance of iron-loaded biochar (BPFSB) derived from sugarcane bagasse and polymerized iron sulfate was investigated, and the mechanism of TC removal was also explored by study of isotherms, kinetics and thermodynamics and characterization of fresh and used BPFSB (XRD, FTIR, SEM and XPS). The results showed that under optimized conditions (initial pH 2; BPFSB dosage 0.8 $g\cdot L^{-1}$; TC initial concentration 100 $mg\cdot L^{-1}$; Contact time 24 h; temperature 298 K), the removal efficiency of TC was as high as 99.03%. The isothermal removal of TC followed well the Langmuir, Freundlich, and Temkin models, indicating that multilayer surface chemisorption dominated the TC removal. The maximum removal capacity of TC by BPFSB at different temperatures was 185.5 $mg\cdot g^{-1}$ (298 K), 192.7 $mg\cdot g^{-1}$ (308 K), and 230.9 $mg\cdot g^{-1}$ (318 K), respectively. The pseudo-second-kinetic model described the TC removal better, while its rate-controlling step was a combination of liquid film diffusion, intraparticle diffusion, and chemical reaction. Meanwhile, TC removal was also a spontaneous and endothermic process, during which the randomness and disorder between the solid–liquid interface was increased. According to the characterization of BPFSBs before and after TC removal, H-bonding and complexation were the major interactions for TC surface adsorption. Furthermore, BPFSB was efficiently regenerated by NaOH. In summary, BPFSB had the potential for practical application in TC removal.

Keywords Bagasse and polymeric ferric sulfate · Iron-loaded biochar · Tetracycline · Adsorption · Potential mechanism

Introduction

Tetracycline (TC) is one of antibiotics widely used in human medicine and animal husbandry (Guo et al. 2019). However, the effective TCs are very few, which results in that more than 80% of TCs or their metabolic derivatives being excreted in urine and feces (Chen et al. 2021). Due to the low removal efficiency of wastewater treatment plants and the stability of TCs, they will accumulate in the aqueous environment (He et al. 2021b; Wei et al. 2022), causing serious damage to human health and ecological ecosystems (Gómez et al. 2022; Li et al. 2022b). Therefore, it is essential to effectively remove TCs from the aqueous environment.

In recent years, several methods have been developed to remove TC from the aqueous environment, including photocatalysis (Shi et al. 2020), electrochemistry (Yang et al. 2020b), membrane methods (Amaly et al. 2021), artificial wetlands (Liu et al. 2019), and adsorption (Liao et al. 2022). Among of them, adsorption is more advantageous because of its simple operation, low cost, and high removal effectiveness (Li et al. 2020). The cost and effectiveness of adsorption depend mainly on the adsorbent. The biochar, activated carbon, carbon nanotube, and graphene oxide could be used as adsorbents (Xu et al. 2022). Comparatively, biochar prepared from industrial or agricultural waste has received more attention for TC removal due to its low cost, high efficiency, and environmental friendliness (Wang et al. 2022). In China, sugarcane is one of the most important raw materials for sugar production, resulting in a large amount of bagasse being produced every year, which

Responsible Editor: Tito Roberto Cadaval Jr

✉ Liheng Liu
deanhenry_liu01@126.com

[1] College of Environmental Science and Engineering, Guilin University of Technology, Guilin 541004, China

[2] Guangxi Key Laboratory of Environmental Pollution Control Theory and Technology, Guilin University of Technology, Guilin 541004, China

[3] Collaborative Innovation Center for Water Pollution Control and Water Safety in Karst Area, Guilin University of Technology, Guilin 541004, China

provides sufficient biomass feedstock for biochar preparation (Raj et al. 2022). Moreover, previous studies have showed that bagasse biochar (BB) performed well for the removal of various organic compounds (Ma et al. 2021; Singh et al. 2022). This predicts that BB is a potential adsorbent for TC removal. However, the adsorption capacity of biochar tends to be lower than that of commercial adsorbents due to low type and number of surface functional groups, low ion exchange capacity, and negative surface charge (Shaheen et al. 2022). Therefore, it is necessary to improve the surface properties of biochar in order to increase its removal efficiency of pollutants.

Many scholars believe that loading metals or metal oxides on the surface of biochar is a feasible approach (Xue et al. 2022). Compared to other metals, iron-loaded biochar has better adsorption performance (Li et al. 2022a). And previous studies have also shown that iron-loaded biochar has good performance for TC removal (Hao et al. 2021; Zhou et al. 2017). There are three methods for the preparation of iron-loaded biochar: co-pyrolysis of iron-containing materials with biomass feedstock; loading iron on the surface of biochar (e.g., liquid-phase reduction); and pyrolysis of iron-rich biomass feedstock. Comparatively, the first method is more promising because the physical and chemical properties of the iron-loaded biochar can be further optimized by controlling the process parameters (Zhang et al. 2022c). Water purification sludge is a by-product of drinking water treatment, which consists mainly of suspended matter, organics, microorganisms and coagulants (Kulandaivelu et al. 2020). Due to the high iron content, it has attracted the attention of researchers as a raw material for the preparation of iron-loaded biochar (Lian et al. 2020).

In our previous work, iron-loaded biochar (BPFSB) was successfully prepared by co-pyrolysis of bagasse and polymerized ferric sulfate (PFS). The maximum adsorption capacity of BPFSB for methylene blue was as high as 128.4 mg/g. Therefore, it is presumed that BPFSB also has a good adsorption capacity for TC. In the present study, the optimized conditions and capacity of BPFSB for TC removal were determined by batch experiments. Meanwhile, the potential pathways and mechanisms of TC removal were explored based on the analysis of experimental data and the characterization of BPFSB. Finally, the regenerative nature of BPFSB was also investigated. The results of this study will provide important technical support and theoretical basis for the application of BPFSB in water treatment.

Materials and methods

Materials

The bagasse (200 mesh) was commercially available, while the TC and PFS were provided by Shanghai Maclean Biochemical Technology Co., Ltd and Tianjin Guangfu Fine Chemical Research Institute, respectively. The other reagents (e.g. NaOH, HCl) were purchased from Xilong Scientific Co., Ltd.

Preparation of biochar

The BPFSB was prepared in the laboratory with the following detailed preparation procedure. First, bagasse and PFS with a mass ratio of 100:1 were thoroughly mixed in ultrapure water. Subsequently, the filtered mixture was dried at 105 °C for 24 h. Then, the dried mixture was heated to 800 °C in a muffle furnace (heating rate: 15 °C/min) and held for 3 h. Finally, the pyrolysis residue after natural cooling was passed through a 100 mesh non-metallic sieve. According to the N_2 adsorption isotherm at 77 K (Beijing High Micro Precision Technology Co., JW-BK200C, China), the specific surface area and pore volume of BPFSB were 407.26 m^2/g and 0.341 cm^3/g, respectively. The zero charge point (pH_{PZC}) of BPFSB determined by mass titration method (Xia et al. 2020) was 7.

Adsorption experiments

First, BPFSB samples with different masses (0.01 g, 0.02 g, 0.03 g, 0.04 g, 0.05 g and 0.1 g) were loaded into centrifugal tubes containing 50 mL of TC solution. The initial concentration (C_0) and pH of TC solution were in the ranges of 50–200 $mg \cdot L^{-1}$ (50 $mg \cdot L^{-1}$, 80 $mg \cdot L^{-1}$, 100 $mg \cdot L^{-1}$, 120 $mg \cdot L^{-1}$, 150 $mg \cdot L^{-1}$, 180 $mg \cdot L^{-1}$ and 200 $mg \cdot L^{-1}$) and 2–12 (2, 4, 6, 8, 10 and 12), respectively. Then, the centrifuge tubes were shaken for 0–24 h (0.08 h, 0.17 h, 0.5 h, 1 h, 2 h, 4 h, 8 h, 12 h, 18 h and 24 h; 200 rpm) at different temperatures (298 K, 308 K and 318 K). Finally, the concentration of TC in the supernatant was determined by UV spectrophotometry at 360 nm. All experiments were performed in triplicate. The removal capacity (q_t, $mg \cdot g^{-1}$) and removal efficiency (φ, %) of TC was calculated by the following equations:

$$q_t = \frac{0.05 \times \left(C_0 - C_t\right)}{W} \tag{1}$$

$$\varphi = \frac{C_0 - C_t}{C_0} \times 100\% \tag{2}$$

where C_0 ($mg \cdot L^{-1}$) and C_t ($mg \cdot L^{-1}$) are the initial concentration and *t*-time concentrations of TC, respectively; *W* (g) is the mass of the BPFSB sample.

Isotherms, kinetics and thermodynamics

In this study, linear Langmuir, Freundlich, Temkin, and D-R models were employed to explore the isotherm of TC removal. Meanwhile, linear pseudo-first-order kinetics model (PFO), pseudo-second-order kinetics model (PSO) and Elovich model were used to study the apparent kinetics of TC removal, while liquid film diffusion model (LFDM), intraparticle diffusion model (IPDM) and chemical reaction model (CRM) were chosen to examine the mass transfer processes of TC removal. Moreover, Gibbs free energy (ΔG, $\mathrm{kJ \cdot mol^{-1}}$), enthalpy change (ΔH, $\mathrm{kJ \cdot mol^{-1}}$) and entropy change (ΔS, $\mathrm{J \cdot mol^{-1} \cdot K^{-1}}$) were used to investigate the thermodynamics of TC removal. The details of these models are shown in Table 1.

Characterization

The crystal structure of BPFSBs was characterized by X-ray diffraction (XRD; PANalyteica, X'Pert3 Power, Netherlands). The scanning range was from 5° to 80°, while the scanning speed was $10° \cdot \mathrm{min^{-1}}$. The surface functional groups were determined by Fourier transform infrared spectrometry (FTIR; Thermo Fisher, Nicolet. iS10, USA). The test method was the potassium bromide compression method, while the scan range, resolution and number of scans were 400–4000 $\mathrm{cm^{-1}}$, 4 $\mathrm{cm^{-1}}$ and 5 times, respectively. The scanning electron microscopy (SEM) with X-ray electron spectroscopy (EDS; HITACHI, SU5000, Japan) was used to investigated surface morphology and elemental distribution of BPFSBs. X-ray photoelectron spectrometer (XPS; Thermo Scientific K-Alpha, USA) was used to explore surface elemental speciation of BPFSBs. The full spectrum was scanned at a flux energy of 100 eV in steps of 1.0 eV, and the narrow spectrum was scanned at a flux energy of 30 eV in steps of 0.1 eV.

Regeneration study

The BPFSB regeneration experiments were also performed in centrifuge tubes. The regeneration agent was NaOH solution (0.1 $\mathrm{mol \cdot L^{-1}}$ and 0.5 $\mathrm{mol \cdot L^{-1}}$). Centrifuge tubes containing 100 mL of NaOH solution and used BPFSB were sonicated for 1.5 h. After centrifugation and separation, the ISBCs were dried to constant weight at 85 °C. The regenerated ISBC was then used to re-adsorb TC under the optimized conditions determined by the adsorption batch experiments. The removal capacity of regenerated BPFSB (q_n, mg/g) was determined according to the method of batch adsorption experiments, and the regeneration efficiency (φ_R, %) was calculated ($\varphi_R = q_n/q_0 \times 100\%$; q_0 (mg/g) is the the initial removal capacity).

Table 1 The details of isotherms models, kinetics models and thermodynamics

Model	Expressions	Parameters
Langmuir	$C_e/q_e = 1/\left(q_{max}k_L\right) + C_e/q_{max}$ $R_L = 1/\left(1 + k_L C_0\right)$	q_e ($\mathrm{mg \cdot g^{-1}}$) is the adsorption capacity of tetracycline at equilibrium; C_e ($\mathrm{mg \cdot L^{-1}}$) is the concentration of TC in solution at equilibrium; q_{max} ($\mathrm{mg \cdot g^{-1}}$) is the maximum adsorption capacity of TC; k_L ($\mathrm{L \cdot mg^{-1}}$) is the Langmuir constant; R_L is separation coefficient。
Freundlich	$lnq_e = lnk_F + 1/n_F lnC_e$	k_F ($\mathrm{mg \cdot g^{-1} \cdot mg^{1/nF} \cdot L^{-1/nF}}$) is the characteristic constant of the Freundlich model; n_F is the constant indicating the adsorption strength or surface heterogeneity
Temkin	$q_e = \frac{RT}{b_T} lnk_T + \frac{RT}{b_T} lnC_e$	T (K) is the Kelvin temperature; R is the ideal gas constant; k_T ($\mathrm{L \cdot mg^{-1}}$) and bT ($\mathrm{kJ \cdot mol^{-1}}$) are the characteristic constants associated with the heat of adsorption
D-R	$\mathrm{lnq_e = lnq_{max} + \beta\varepsilon^2}$ $\mathrm{\varepsilon = RTln\left(1 + 1/C_e\right)}$ $\mathrm{E = 1/\sqrt{2\beta}}$	β ($\mathrm{mol^2 \cdot kJ^{-2}}$) is a constant related to the adsorption energy (E); ε (kJ/mol) is the adsorption potential
PFO	$ln\left(q_e - q_t\right) = lnq_e - k_1 t$	k_1 ($\mathrm{h^{-1}}$) is the pseudo-first-order rate constant. q_t ($\mathrm{mg \cdot g^{-1}}$) is the amount of adsorption at time t
PSO	$\frac{t}{q_t} = \frac{1}{k_2 q_e^2} + \frac{t}{q_e}$	k_2 ($\mathrm{g \cdot mg^{-1} \cdot h^{-1}}$) is the pseudo-second-order rate constant
Elovich	$q_t = \frac{1}{\beta} ln(\alpha\beta) + \frac{1}{\beta} lnt$	α ($\mathrm{mg \cdot h^{-1}}$) is the initial removal rate; β ($\mathrm{g \cdot mg^{-1}}$) is a constant related to the surface coverage and activation energy
LDF	$\ln\left(1 - \frac{q_t}{q_e}\right) = -k_{LF} t + A$	k_{LF} ($\mathrm{h^{-1}}$) is the diffusion rate constant; A is the diffusion constant
IPD	$q_t = k_{IP} t^{0.5} + C$	k_{ID} ($\mathrm{g \cdot mg^{-1} \cdot h^{0.5}}$) is the diffusion rate constant; C is the boundary characteristic constant
CR	$\ln = \left(1 - \frac{q_t}{q_e}\right)^{1/3} = k_C t$	k_C ($\mathrm{h^{-1}}$) is the chemical reaction rate constant
Thermody-namics	$\Delta G = \Delta H - T\Delta S$ $\Delta G = -RT\ln k_L$	ΔG ($\mathrm{kJ \cdot mol^{-1}}$) is the Gibbs free energy change, ΔH ($\mathrm{kJ \cdot mol^{-1}}$) is the enthalpy change, ΔS ($\mathrm{J \cdot mol^{-1} \cdot K^{-1}}$) is the entropy change

Statistical analysis

In this work, residual root-mean-squared error (RMSE) and chi-square test (χ^2) were used to assess consistency between experimental data ($q_{\mathrm{i.exp}}$) and model prediction data ($q_{\mathrm{i.cal}}$). Their expressions are as follows:

$$RMSE = \sqrt{\frac{1}{N-P}\sum_{i=1}^{N}\left(q_{i,\exp} - q_{i,\mathrm{cal}}\right)^2} \tag{3}$$

$$x^2 = \sum_{i=1}^{N}\frac{\left(q_{i,\exp} - q_{i,\mathrm{cal}}\right)^2}{q_{i,\mathrm{cal}}} \tag{4}$$

where N is the number of experimental data, P is the number of model parameters.

Results and discussion

Effect of different parameters on TC removal

Initial pH

In general, the initial pH of the solution significantly affects the removal performance of the adsorbent for adsorbates because it determines the surface properties of the adsorbent and the species forms of the adsorbate. When the initial pH is less than 7 or $\mathrm{pH_{PZC}}$, the surface of the adsorbent is positively charged, while the surface of the adsorbent tends to be negatively charged when the initial pH is greater than 7 or $\mathrm{pH_{PZC}}$ (Liu et al. 2020). The TC in solution usually has four forms depending on the pH: $\mathrm{TC^+}$ ($\mathrm{pH} < 3.3$), $\mathrm{TC^0}$ ($3.3 < \mathrm{pH} < 7.7$), $\mathrm{TC^-}$ ($7.7 < \mathrm{pH} < 9.3$) and $\mathrm{TC^{2-}}$ ($\mathrm{pH} > 9.3$) (Sun et al. 2022). Therefore, the removal capacity of biochar for TC should theoretically fluctuate at different initial pH values due to the electrostatic interaction (Wu et al. 2022). However, the removal capacity and removal efficiency of TC shown in Fig. 1a trended continuous decrease with the increase of initial pH in the studied range. When the initial pH was raised from 2 to 12, the removal capacity was decreased from 142.2 mg·g $^{-1}$ to 79.45 mg·g^{-1}, while corresponding removal efficiency was declined from 85.32% to 47.67%, suggesting that the electrostatic interactions was non-dominant for the TC removal by BPFSB, and that the role of other adsorption mechanisms (e.g. hydrogen bonding, π-π interaction, pore filling, etc.) was more significant.

BPFSB dosage

The dosage of adsorbent is usually related to the efficiency and cost of pollutant removal. The effect of BPFSB dosage on TC removal is shown in Fig. 1b. As the dosage of BPFSB increased from 0.2 g·L^{-1} to 2.0 g·L^{-1}, the TC adsorption capacity decreased from 178.0 mg·g^{-1} to 49.94 mg·g^{-1}. This was due to the fact that high doses of BPFSB produced aggregation of particles, resulting in overlapping of adsorption sites, reduction of effective surface area (Xu et al. 2019), and prolongation of TC diffusion paths (Zhang et al. 2022b). However, the removal efficiency of TC increased from 35.61% to 99.89% with the increase of BPFSB dose, which should be attributed to that the higher dose of BPFSB provided more contact area and adsorption sites (Song et al. 2022a, b). It was of interest that the TC removal efficiency was as high as 99.03% at a BPFSB dose of 0.8 g·L^{-1}, suggesting that 0.8 g·L^{-1} should be an economic dosage for TC removal.

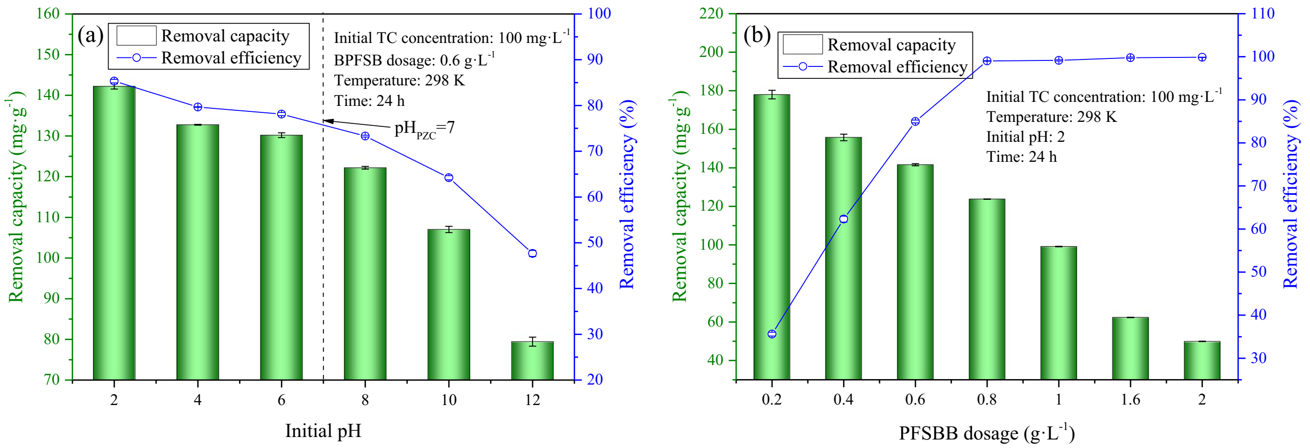

Fig. 1 Effect of initial pH (**a**) and BPFSB dose (**b**) on TC removal

Adsorption isotherms and thermodynamics

Isotherms

The isothermal removal performance of BPFSB for TC and its fitting plots are shown in Fig. 2, while the corresponding fitting parameters are listed in Table 2. As shown in Fig. 2a, The TC removal capacity of BFSBC was significantly increased with the increase of TC initial concentration and temperature. This may be due to the following reasons: 1) higher TC concentrations had greater mass transfer force, resulting in rapid migration to BPFSB surface of more TC (Zheng et al. 2021); 2) the high temperature enhanced the thermal motion (Brownian motion) of the TC molecules and reduced the viscosity of the solution, resulting in an increased opportunity for contact with BFSBC (Sun et al. 2019); 3) the temperature rise activated the adsorption sites, which facilitated the formation of iron-antibiotic complex (Song et al. 2020).

Due to the highest R^2 values and the lowest χ^2 and *RMSE* values, the Temkin model best described the isothermal removal of TC by BPFSB, indicating that the removal of TC was dominated by chemisorption, and that the heat of adsorption was linearly decreased with increasing surface coverage of BPFSB (Zeng and Kan 2022). Since R^2 values were higher than 0.98, the Langmuir and Freundlich models also described the TC removal very well, suggesting that the mechanism of TC

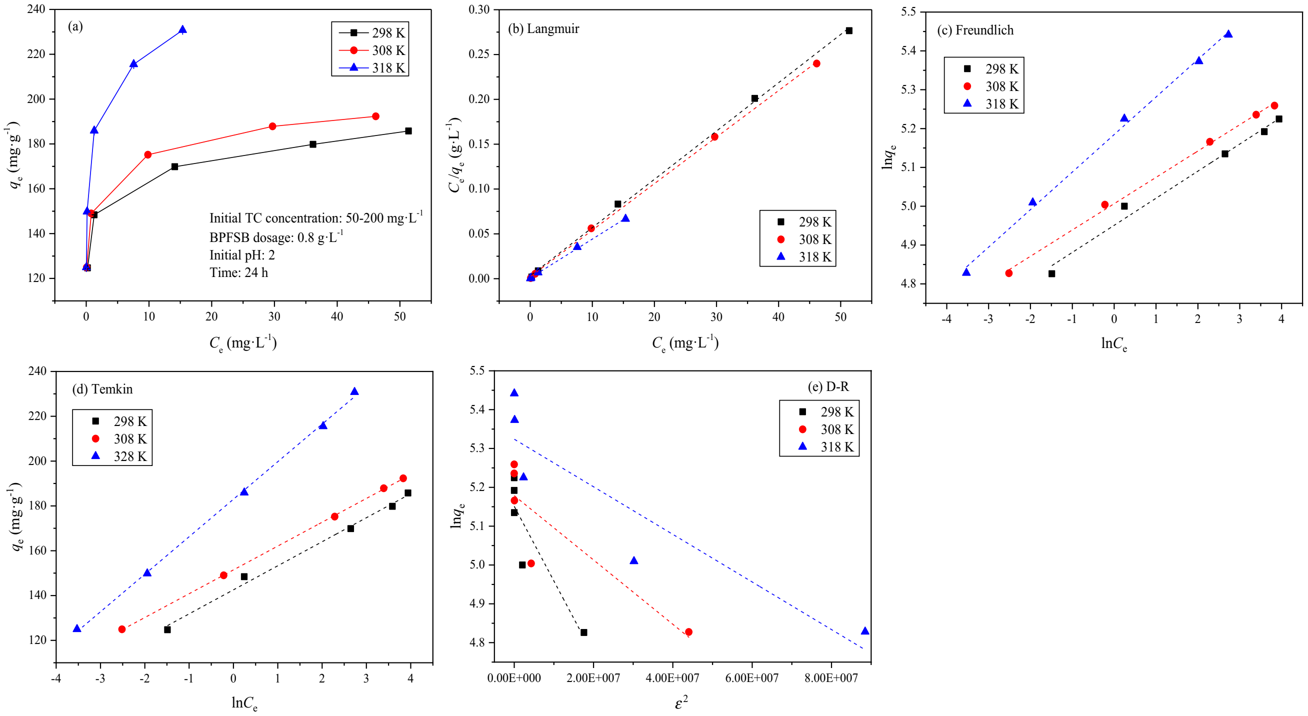

Fig. 2 Isothermal removal and fitting plots of TC by BPFSB

Table 2 The fitting parameters of Langmuir, Freundlich, Temkin and D-R models

T(K)	Langmuir model					Freundlich model					
	q_{max}(mg·g^{-1})	k_L (L·mg^{-1})	R^2	χ^2	RMSE	n_F	k_F (mg·g^{-1}·mg$^{1/nF}$·L$^{-1/nF}$)	R^2		χ^2	RMSE
298	185.5	1.739	0.9990	104.1	43.78	14.34	141.3	0.9807		0.2222	3.247
308	192.7	2.370	0.9994	288.6	56.05	14.76	149.4	0.9970		0.0452	1.528
318	230.9	5.166	0.9984	323.1	63.07	10.35	178.5	0.9959		0.1317	2.738
T(K)	Temkin model					D-R model					
	b_T(kJ·mol^{-1})	k_T (L·mg^{-1})	R^2	χ^2	RMSE	q_{max}(mg·g^{-1})	β	E (kJ·mol^{-1})	R^2	χ^2	RMSE
298	230.9	5.89E+05	0.9907	0.1196	2.418	172.6	1.92E-08	50.98	0.7518	3.220	13.45
308	240.8	1.53E+06	0.9998	0.0028	0.399	177.4	8.28E-09	77.69	0.7016	4.800	16.66
318	157.9	5.58E+04	0.9985	0.0459	1.727	205.2	6.13E-09	90.33	0.7832	7.844	22.33

removal by BPFSB may be as follows (Zhu et al. 2022): 1) the binding of TC on the homogeneous surface of BPFSB was monolayer, resulting in the continuous generation of a "new adsorbent"; 2) When the removal of TC was close to saturation, van der Waals forces would be dominant in the interaction between TC and BPFSB. Moreover, the separation coefficient R_L and the separation intensity ($1/n_F$) were in the range of 0–1, indicating that the removal of TC by BPFSB was favorable. In addition, the R^2 values of the D-R models were all less than 0.8, suggesting that the contribution of pore filling to TC removal was insignificant. Meanwhile, the E values at different temperature were 50.98 kJ·mol^{-1} (298 K), 77.69 kJ·mol^{-1} (308 K), and 90.33 kJ·mol^{-1} (318 K), demonstrating that TC removal by BPFSB was primarily controlled by chemisorption (Yuan et al. 2021). According to the Langmuir model, the maximum removal amounts of TC by BPFSB were 185.5 mg·g^{-1} (298 K), 192.7 mg·g^{-1} (308 K), and 230.9 mg·g^{-1} (318 K), respectively, which were much higher than the adsorbents reported in previous studies (Table 3).

Thermodynamics

The thermodynamic parameters are listed in Table 4. The negative ΔG indicated that the removal of TC by BPFSB was spontaneous, while the increasingly negative ΔG with increasing temperature suggested that the process was thermodynamically feasible (Yu et al. 2020). The absolute value of ΔG at 318 k was much higher than those of other temperatures, which may be due to the generation of a large amount of Fe-TC complexes (Song et al. 2020). The ΔH values was greater than 40 kJ·mol^{-1}, declaring that the removal of TC by BPFSB was an endothermic process dominated by chemisorption (Güleç et al. 2022). In addition, the positive ΔS evidenced that the randomness and disorder between the solid–liquid interface was increased during TC removal by BPFSB (Yang et al. 2020a).

Table 4 Thermodynamic parameters for TC adsorption on BPFSB

Temperature (K)	ΔG (kJ·mol^{-1})	ΔH (kJ·mol^{-1})	ΔS (J·mol^{-1}·K^{-1})
298	-1.370	43.11	148.5
308	-2.209		
318	-4.341		

Adsorption kinetics

The removal capacity of TC at different contact times and its fitting plots are shown in Fig. 3, while their corresponding kinetic parameters are listed in Table 5. As shown in Fig. 3a, the removal capacity of TC increased with the increase of contact time. However, this increasing trend became very slight when the contact time was greater than 18 h, predicting that 18 h could be considered as the equilibrium time. Comparing the fitting results of the PFO and PSO (Fig. 3c and Fig. 3b), the removal of TC by BPFSB better followed the PSO because of greater R^2 value and lower χ^2 and $RMSE$ values (Table 5), predicting that the removal of TC was mainly dependent on the chemisorption (Xiang et al. 2022), which likely involved the exchange, transfer and sharing of electrons (Jiang et al. 2023). In addition, due to the higher R^2 value (0.9836) and the minimum χ^2 (0.5001) and RMSE (2.646) values, the TC removal could also be well described by the Elovich model, indicating that the TC removal dominated by chemisorption was heterogeneous (Omidi et al. 2022). Meanwhile, α was much higher than β, suggesting that the adsorption between BPFSB and TC was very effective (Zhang et al. 2022a).

According to Fig. 3e, Fig. 3f and Fig. 3g, the removal of TC could be divided into three stages: fast removal stage (1st stage; 0–2 h), slow removal stage (2nd stage; 2–12 h) and asymptotic saturation stage (3rd stage; 12–24 h). In the first stage, TC rapidly migrated to the surface of BPFSB and bound to the sufficient adsorption sites due to the large concentration difference between solid and liquid phases. Subsequently, the reduction of the concentration difference

Table 3 Comparison with adsorbents in previous studies

Raw materials	Additives	Preparation methods	pH and temperature (K)	q_t (mg·g^{-1})	Reference
bagasse	polymerized ferric sulfate	co-pyrolysis	pH = 2.0, T = 298, 308, 318	185.5 192.7 230.9	This study
sawdust	$FeCl_3·6H_2O$	co-pyrolysis	pH = 6.0, T = 298	102	Zhou et al. (2017)
hazelnut shell	$FeCl_3$	co-pyrolysis	pH = 6.5, T = 298	48.3	Hao et al. (2021)
rice straw	$FeCl_3·6H_2O$ + urea	co-pyrolysis	T = 298	156	Mei et al. (2021)
sewage sludge	$(NH_4)_2Fe(SO_4)_2·6H_2O$	hydrothermal carbonisation	pH = 6.0, T = 293.15	104.86	Wei et al. (2019)
chicken bone	$FeCl_3·6H_2O + FeSO_4.7H_2O$	co-precipitation	pH = 8.0–10.0, T = 299.15	98.89	Oladipo and Ifebajo (2018)

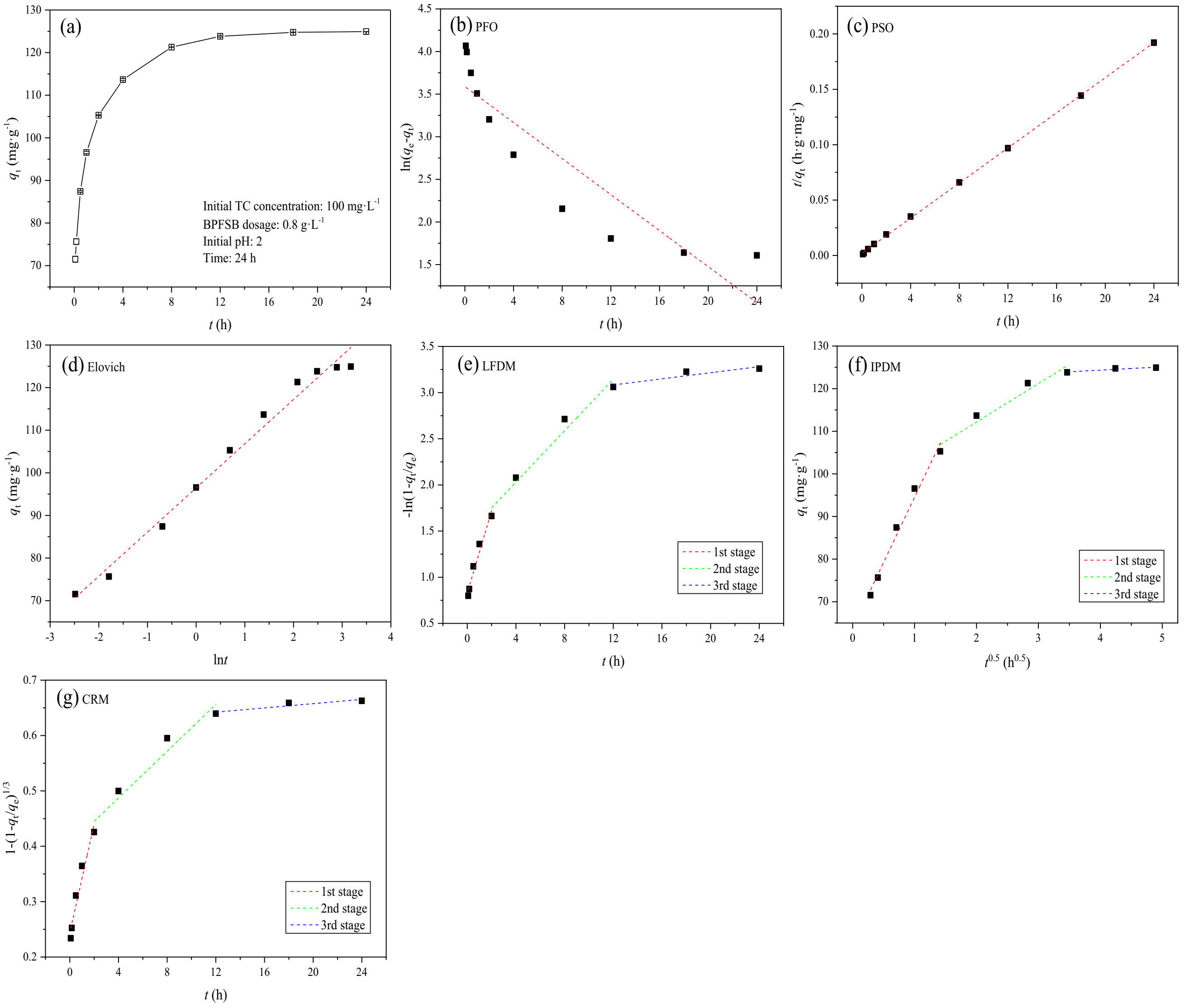

Fig. 3 Effect of contact time on TC removal capacity and its fitting plots by different kinetic models

Table 5 Kinetic parameters for TC adsorption on BPFSB

PFO				PSO				Elovich			
Parameters	Values			Parameters	Values			Parameters	Values		
$q_{e,cal}$ (mg·g^{-1})	36.20			$q_{e,cal}$ (mg·g^{-1})	126.1			α (mg·h^{-1})	1.14E+05		
k_1 (h^{-1})	0.1057			k_2 (g·mg^{-1}·h^{-1})	0.0314			β (g·mg^{-1})	0.0964		
R^2	0.7996			R^2	0.9998			R^2	0.9836		
χ^2	3.48E+04			χ^2	65.47			χ^2	0.5001		
RMSE	102.1			RMSE	17.19			RMSE	2.646		
LFDM				IPDM				CRM			
Parameters	Value1	Value2	Value3	Parameters	Value1	Value2	Value3	Parameters	Value1	Value2	Value3
k_{LF} (h^{-1})	0.4439	0.1394	0.0166	k_{ID} (g·mg^{-1}·h$^{0.5}$)	30.60	9.033	0.7775	k_{CR} (h^{-1})	0.0979	0.0211	0.0019
A_L	0.8297	1.473	2.884	A_I	63.92	94.10	121.2	A_C	0.2440	0.4029	0.6190
R^2	0.9471	0.9584	0.7882	R^2	0.9776	0.9293	0.7882	R^2	0.9244	0.9262	0.7362
χ^2	0.4363	0.0588	6.71E-4	χ^2	0.1469	0.0852	5.93E-4	χ^2	0.5697	0.0944	7.03E-4
RMSE	3.468	1.806	0.2891	RMSE	2.110	2.220	0.2718	RMSE	3.989	2.299	0.2959

and the decline of the effective adsorption sites led to the decrease of the diffusion rate of TC (liquid film diffusion and intraparticle diffusion), resulting in the weakening of the binding ability of TC to the adsorption sites. When the contact time was extended from 12 to 24 h, the removal efficiency of TC only increased from 99.06% to 99.94%, which indicated that the adsorption was basically equilibrium. As shown in Table 3, the differences in R^2 values for the different stages of the LFDM, IPDM and CRM were negligible, and the corresponding A_L, A_I and A_C values were also nonzero, indicating that the removal rate of TC was determined by a combination of liquid film diffusion, intra-particle diffusion and chemical reaction (or chemical interaction).

Characterization of biochar before and after TC removal

XRD

As shown in Fig. 4a, the crystal structure of BPFSB before TC adsorption was mainly quartz (2θ = 20.81°, 26.56°, 36.51°, 39.44°, 50.06°, 59.95° and 68.25°) (He et al. 2021a; Liang et al. 2017), which attributed to the transformation of silica elements in bagasse at high temperatures (Hassan et al. 2020). Moreover, the broad peak around 2θ = 22.7° related to amorphous carbon structure originated from the pyrolysis of lignin and cellulose (Alchouron et al. 2020). In addition, the characteristic peak of Fe^0 (2θ = 44.3° and 64.6°) (Zhang et al. 2021) was also observed, indicating that the co-pyrolysis of bagasse and PFS may result in the reduction of Fe^{3+}. (Song et al. 2022a, b). However, no characteristic peaks for other Fe-containing substances were found, which may be due to the following reasons (Ndagijimana et al. 2022; Wen et al. 2022): 1) the distribution of Fe-containing substances was uniform, and their particle size was tiny; 2) the Fe-containing substances were in non-crystalline or low-crystalline state. After the adsorption of TC, the intensity of Fe^0 characteristic peaks was significantly decreased, and there were new characteristic peaks detected at 2θ = 35.75° and 41.7° which were associated with Fe_3O_4 and FeO, respectively. This phenomenon suggested that Fe(0) may have chemical reactions with TC.

FTIR

According to the FTIR spectrum (Fig. 4b), the functional groups on the BPFSB surface are mainly -OH (3430 cm^{-1}), methyl and methylene -CH (2923 cm^{-1}, 2852 cm^{-1}), C = C/C = O (1590 cm^{-1}), C-O (1100 cm^{-1}), aromatic cyclic -CH (780 cm^{-1}) and Fe–O (560 cm^{-1}) (Gan et al. 2020; Hu et al. 2021; Pi et al. 2019; Tang et al. 2022; Zhao et al. 2019), The characteristic Fe–O peak indicated the presence of iron oxides on the BPFSB surface, which confirmed that the iron oxides presented in a low crystalline or amorphous form. After the adsorption of TC, the characteristic peak representing Fe–O was almost disappeared, and a new characteristic peak referring to C = O was appeared at 1720 cm^{-1} (Wu et al. 2019). Meanwhile, there was a slight shift for the characteristic peak of -OH. These indicated that the mechanism of TC removal may involve H-bonding and complexation (Ma et al. 2022).

SEM

As shown in Fig. 5, the pores of BPFSB were obviously narrowed, and nitrogen elements was appeared on its surface. Meanwhile, the distribution of nitrogen elements was almost the same pattern as that of Fe elements and oxygen elements, indicating that TC may complex with Fe oxides on

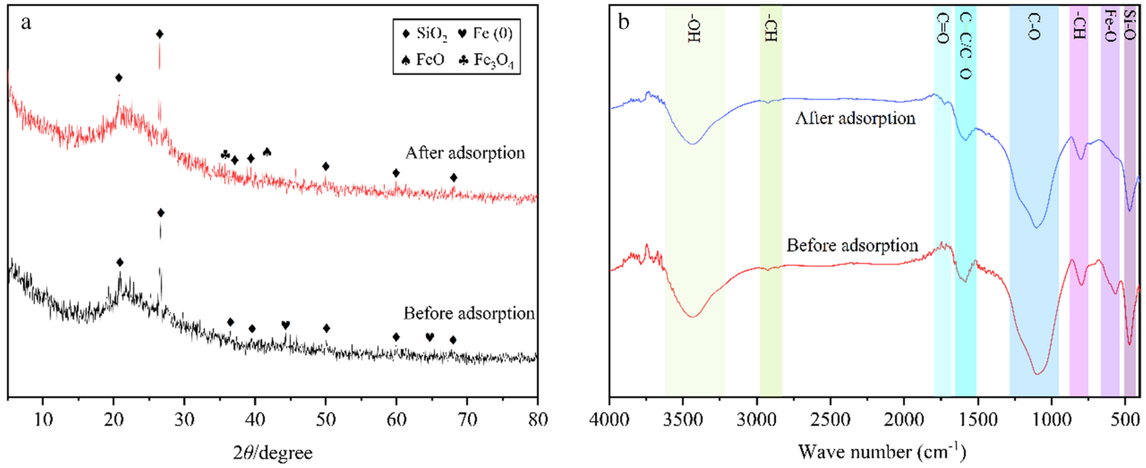

Fig. 4 XRD patters (**a**) and FTIR spectra (**b**) of BPFSB before and after adsorption

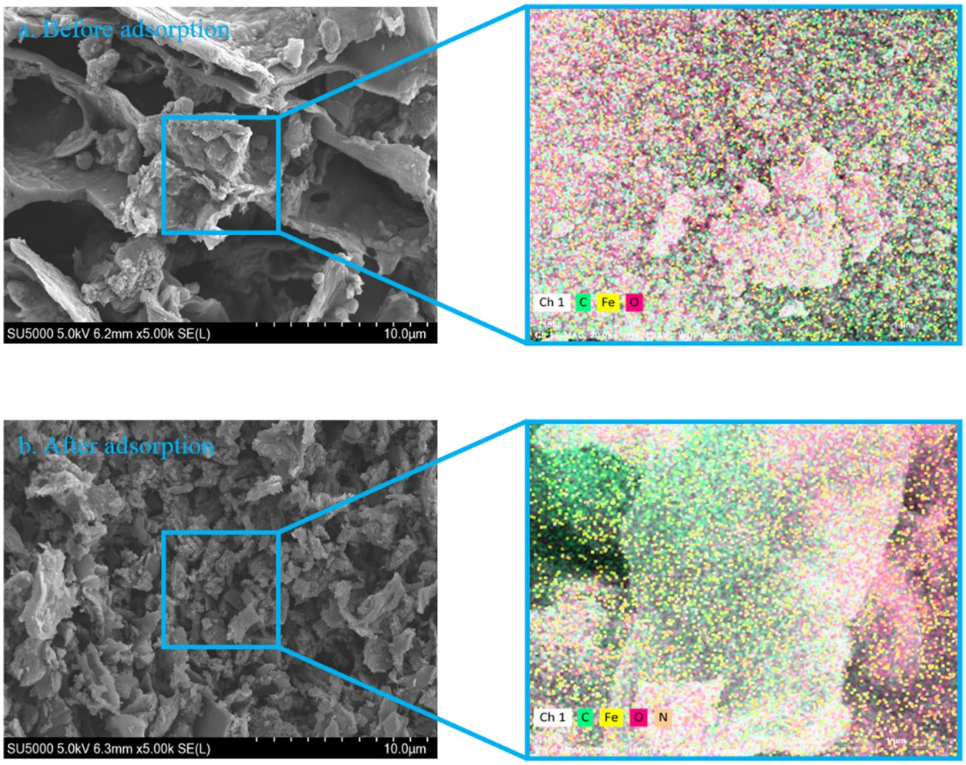

Fig. 5 SEM images and the element distribution mappings of BPFSB before and after adsorption

the surface of BPFSB, and that TC may also combine with oxygen-containing functional groups through H-bonding.

XPS

The XPS spectra of BPFSB before and after adsorption are shown in Fig. 6. The full-scan spectrum showed a significant increase in the intensity of the characteristic peak representing N1*s* after TC adsorption (Fig. 6a), indicating that TC was successfully attached to the BPFSB. As shown in Fig. 6b, the characteristic peaks representing C-O, C=O and COO/C–O–C were significantly shifted and their proportions were also reduced after TC adsorption, which may be attributed to strong H-bonding interactions (Jin et al. 2019; Wang et al. 2021b). Comparing the fine scan spectra of O1*s* (Fig. 6c), the most significant differences before and after TC adsorption involved two aspects: 1) the intensity of the characteristic peaks associated with Fe–O and COO/C–O–C was weakened; 2) the positions of the characteristic peaks related to Fe–O, C=O, C-O/Si–O and COO/C-O were shifted. These confirmed the important contribution of H-bonding and complexation to the removal of TC (Li et al. 2021; Mei et al. 2021; Wang et al. 2021a). As shown in Fig. 6d, there were three forms of Fe 2*p*: zero-valent iron (Fe^0), divalent iron (Fe^{2+}) and trivalent iron (Fe^{3+}). Their proportions were 16.47%, 33.46% and 50.06% before TC adsorption. After TC adsorption, the proportion of Fe^0 and Fe^{3+} were individually decreased to 1.73% and 31.38%, while the proportion of Fe^{2+} was increased to 66.89%. These predicted that both Fe^0 and Fe^{3+} should react with TC.

Potential mechanisms of TC removal

Based on the analysis of experimental data and the characterization of BPFSB, the potential pathways and mechanisms of TC removal by BPFSB were proposed (Fig. 7). First, TC crossed the liquid film and diffused to the surface of BPFSB due to the TC concentration difference between the solid–liquid interface (liquid film diffusion). Subsequently, TC migrated to the blank adsorption sites on the surface of BPFSB and bound with them (surface adsorption). When the adsorption sites on the surface were occupied in large quantities, TC would diffuse to the pores (pore filling). Among them, surface adsorption was dominant.

The details of the surface adsorption of TC on BPFSB were as follows. When TC diffused to the adsorption sites, TC bound with them via H-bonding, complexation, π-π interactions, electrostatic interactions and van der Waals forces, while H-bonding and complexation may be the main roles. At the same time, TC would react with Fe^0 and Fe^{3+} on the surface of BPFSB and produced intermediates (Eq. (4) ~ Eq. (7)). These intermediates then bound with the adsorption sites by the above actions.

$$Fe^0 + H^+ \rightarrow Fe^{2+} + [H] \tag{4}$$

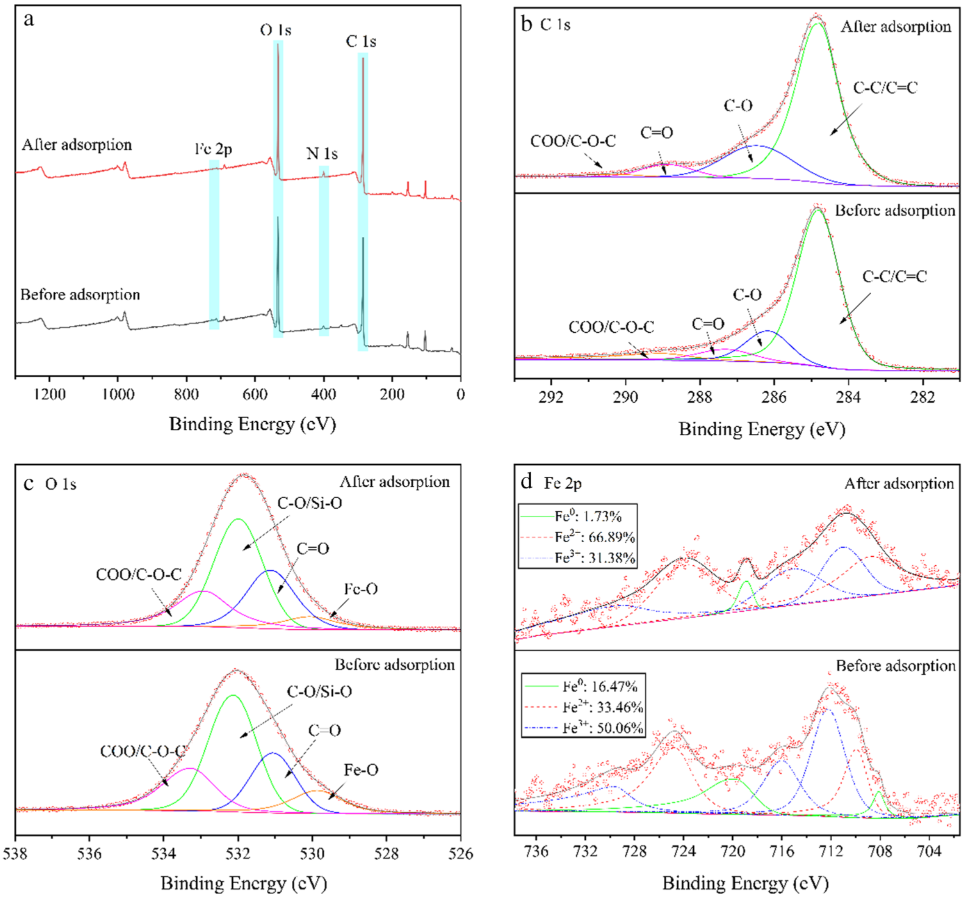

Fig. 6 XPS spectra of BPFSB before and after TC removal

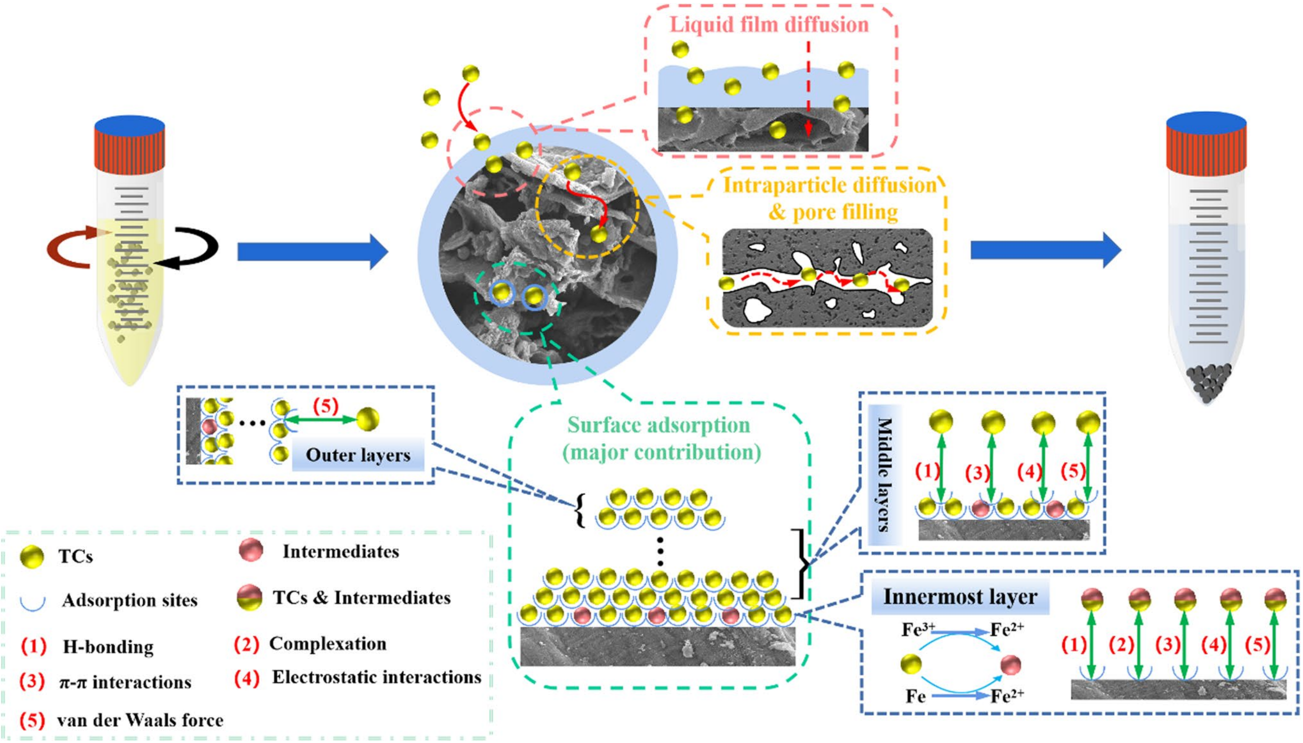

Fig. 7 Potential pathways and mechanisms of TC removal by BPFSB

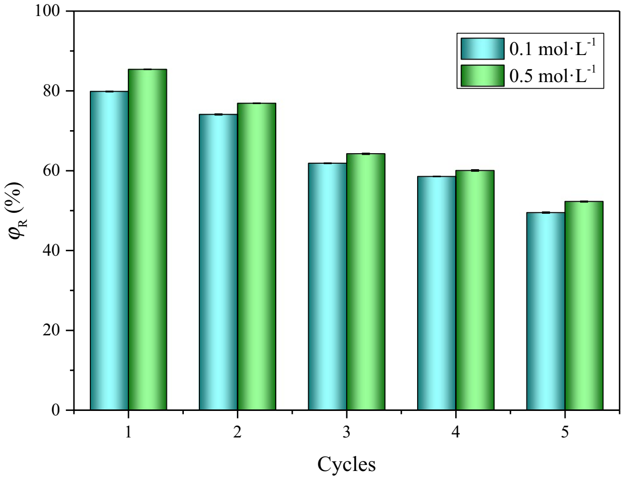

Fig. 8 Regeneration Performance of BPFSB

$$[\mathrm{H}] + \mathrm{TC} \rightarrow \mathrm{intermediate} \tag{5}$$

$$\mathrm{Fe}^{3+} + \mathrm{TC} \rightarrow \mathrm{Fe}^{3+} - \mathrm{TC(complex)} \tag{6}$$

$$\mathrm{Fe}^{3+} + \mathrm{TC} + [\mathrm{H}] \rightarrow \mathrm{Fe}^{2+} + \mathrm{intermediate} \tag{7}$$

When the monolayer adsorption on the surface of BPFSB was completed, a new adsorbent was formed. Subsequently, TC migrated to the adsorption sites on the new adsorbent surface and continued the monolayer adsorption. The interactions of TC with the new adsorbent may be H-bonding, π-π interaction, electrostatic interaction and van der Waals forces, among which the contribution of H-bonding may be more significant. The above processes were repeated until the saturation state was approached. Finally, the main interaction of TC attachment to the adsorbent was van der Waals force (physical adsorption).

Regeneration

The regeneration performance is very important for the practical application of adsorbent. As shown in Fig. 8, the regeneration efficiency of BPFSB was higher (74.11% ~ 85.40%) in cycles 1–2, while in cycles 3–5, the regeneration efficiency of ISBC was significantly lower (49.51% ~ 64.25%). These above may be due to the accumulation of TC on the surface of BPFSBs and the longer exposure of the ISBC surface to the regeneration agents (Zeng et al. 2021). Moreover, the regeneration effectiveness of 0.5 mol·L^{-1} NaOH solution was better. Compared with previous studies (Li et al. 2022c; Zhu et al. 2022), the regeneration performance of BPFSB was still acceptable, indicating that it had potential for practical applications.

Conclusion

BPFSB was an adsorbent with superior removal capacity for TC. When the initial pH was 2 and the dose of BPFSB was 0.8 g/L, the removal efficiency of TC was as high as 99.03%. The maximum removal amounts of TC by BPFSB at different temperatures were 185.5 mg·g^{-1} (298 K), 192.7 mg·g^{-1} (308 K) and 230.9 mg·g^{-1} (318 K), respectively. The isothermal removal of TC by BPFSB followed the Langmuir, Freudlich and Temkin model well, indicating that the removal of TC was multilayer adsorption dominated by chemisorption, and the contribution of surface adsorption was major. The pseudo-second-kinetic model described the process better, and the liquid film diffusion, intraparticle diffusion and chemical reaction together determined the TC removal rate. Thermodynamic analysis indicated that the TC removal was a spontaneous and endothermic process, and the randomness and disorder between the solid–liquid interface was increased. In addition, the characterization of BPFSB suggested that TC was mainly attached to the adsorbent surface through H-bonding and complexation. Furthermore, BPFSBs could be effectively regenerated by NaOH. In summary, BPFSBs had the potential to be practically applicable for TC removal.

Author contributions Qiaojing Liu: Conceptualization, Methodology, Writing—Original Draft. Xinfeng Cao: Validation, Visualization. Tiantian Yue: Validation, Visualization. Fengzhi Zhang: Validation, Visualization. Shaoyuan Bai: Resources, Supervision, Funding acquisition, Project administration. Liheng Liu: Conceptualization, Methodology, Resources, Writing—Original Draft, Writing—Review & Editing, Supervision, Funding acquisition.

Funding This work was supported by Guangxi Key R&D Program Project (Guike AB21220006), National Natural Science Foundation of China (52160016), Guangxi Key Laboratory of Environmental Pollution Control Theory and Technology Fund Project (Guikeneng1801Z009), the project of high level innovation team and outstanding scholar in Guangxi colleges and universities (002401013001), and Guangxi Key Laboratory of Environmental Pollution Control Theory and Technology for Science and Education Combined with Science and Technology Innovation Base.

Data availability The data-set used and/or analyzed during this study are available from the corresponding author on reasonable request.

Declarations

Ethical approval This article does not contain any studies with human participants or animals performed by any of the authors.

Consent to participate None of the authors has any objection to participating in the study.

Consent for publication All authors agreed with the content all gave explicit consent to submit and they obtained consent from the responsible authorities at the institute/organization where the work has been carried out before the work is submitted.

Competing interests The authors have no relevant financial or non-financial interests to disclose.

References

Alchouron J, Navarathna C, Chludil HD, Dewage NB, Perez F, Hassan EB, Pittman CU Jr, Vega AS, Mlsna TE (2020) Assessing South American Guadua chacoensis bamboo biochar and Fe3O4 nanoparticle dispersed analogues for aqueous arsenic(V) remediation. Sci Total Environ 706:135943. https://doi.org/10.1016/j.scitotenv.2019.135943

Amaly N, El-Moghazy AY, Sun G, Pandey PK (2021) Effective tetracycline removal from liquid streams of dairy manure via hierarchical poly (vinyl alcohol-co-ethylene)/polyaniline metal complex nanofibrous membranes. J Colloid Interface Sci 597:9–20. https://doi.org/10.1016/j.jcis.2021.03.165

Chen W, Zhao B, Guo Y, Guo Y, Zheng Z, Pak T, Li G (2021) Effect of hydrothermal pretreatment on pyrolyzed sludge biochars for tetracycline adsorption. J Environ Chem Eng 9:106557. https://doi.org/10.1016/j.jece.2021.106557

Gan Q, Hou H, Liang S, Qiu J, Tao S, Yang L, Yu W, Xiao K, Liu B, Hu J, Wang Y, Yang J (2020) Sludge-derived biochar with multivalent iron as an efficient Fenton catalyst for degradation of 4-Chlorophenol. Sci Total Environ 725:138299. https://doi.org/10.1016/j.scitotenv.2020.138299

Gómez E, Cestaro R, Philippe L, Serrà A (2022) Electrodeposition of nanostructured Bi2MoO6@Bi2MoO6–x homojunction films for the enhanced visible-light-driven photocatalytic degradation of antibiotics. Appl Catal B-Environ 317:121703. https://doi.org/10.1016/j.apcatb.2022.121703

Güleç F, Williams O, Kostas ET, Samson A, Stevens LA, Lester E (2022) A comprehensive comparative study on methylene blue removal from aqueous solution using biochars produced from rapeseed, whitewood, and seaweed via different thermal conversion technologies. Fuel 330:125428. https://doi.org/10.1016/j.fuel.2022.125428

Guo X, Mu Q, Zhong H, Li P, Zhang C, Wei D, Zhao T (2019) Rapid removal of tetracycline by Myriophyllum aquaticum: Evaluation of the role and mechanisms of adsorption. Environ Pollut 254:113101. https://doi.org/10.1016/j.envpol.2019.113101

Hao D, Chen Y, Zhang Y, You N (2021) Nanocomposites of zero-valent iron@biochar derived from agricultural wastes for adsorptive removal of tetracyclines. Chemosphere 284:131342. https://doi.org/10.1016/j.chemosphere.2021.131342

Hassan M, Liu Y, Naidu R, Parikh SJ, Du J, Qi F, Willett IR (2020) Influences of feedstock sources and pyrolysis temperature on the properties of biochar and functionality as adsorbents: A meta-analysis. Sci Total Environ 744:140714. https://doi.org/10.1016/j.scitotenv.2020.140714

He L, Lv L, Pillai SC, Wang H, Xue J, Ma Y, Liu Y, Chen Y, Wu L, Zhang Z, Yang L (2021) Efficient degradation of diclofenac sodium by periodate activation using Fe/Cu bimetallic modified sewage sludge biochar/UV system. Sci Total Environ 783:146974. https://doi.org/10.1016/j.scitotenv.2021.146974

He X, Kai T, Ding P (2021b) Heterojunction photocatalysts for degradation of the tetracycline antibiotic: a review. Environ Chem Lett 19:4563–4601. https://doi.org/10.1007/s10311-021-01295-8

Hu Y, Chen D, Zhang R, Ding Y, Ren Z, Fu M, Cao X, Zeng G (2021) Singlet oxygen-dominated activation of peroxymonosulfate by passion fruit shell derived biochar for catalytic degradation of tetracycline through a non-radical oxidation pathway. J Hazard Mater 419:126495. https://doi.org/10.1016/j.jhazmat.2021.126495

Jiang YC, Luo MF, Niu ZN, Xu SY, Gao Y, Gao Y, Gao WJ, Luo JJ, Liu RL (2023) In-situ growth of bimetallic FeCo-MOF on magnetic biochar for enhanced clearance of tetracycline and fruit preservation. Chem Eng J 451:138804. https://doi.org/10.1016/j.cej.2022.138804

Jin J, Yang Z, Xiong W, Zhou Y, Xu R, Zhang Y, Cao J, Li X, Zhou C (2019) Cu and Co nanoparticles co-doped MIL-101 as a novel adsorbent for efficient removal of tetracycline from aqueous solutions. Sci Total Environ 650:408–418. https://doi.org/10.1016/j.scitotenv.2018.08.434

Kulandaivelu J, Choi PM, Shrestha S, Li X, Song Y, Li J, Sharma K, Yuan Z, Mueller JF, Wang C, Jiang G (2020) Assessing the removal of organic micropollutants from wastewater by discharging drinking water sludge to sewers. Water Res 181:115945. https://doi.org/10.1016/j.watres.2020.115945

Li A, Ge W, Liu L, Qiu G (2022) Preparation, adsorption performance and mechanism of MgO-loaded biochar in wastewater treatment: A review. Environ Res 212:113341. https://doi.org/10.1016/j.envres.2022.113341

Li S, Huang W, Yang P, Li Z, Xia B, Li M, Xue C, Liu D (2021) One-pot synthesis of N-doped carbon intercalated molybdenum disulfide nanohybrid for enhanced adsorption of tetracycline from aqueous solutions. Sci Total Environ 754:141925. https://doi.org/10.1016/j.scitotenv.2020.141925

Li X, Wang C, Zhang J, Liu J, Liu B, Chen G (2020) Preparation and application of magnetic biochar in water treatment: A critical review. Sci Total Environ 711:134847. https://doi.org/10.1016/j.scitotenv.2019.134847

Li Y, Cao H, Liu W, Liu P (2022) Effective degradation of tetracycline via recyclable cellulose nanofibrils/polyvinyl alcohol/Fe3O4 hybrid hydrogel as a photo-Fenton catalyst. Chemosphere 307:135665. https://doi.org/10.1016/j.chemosphere.2022.135665

Li Z, Wang Y, Zheng S, Qian P, Zhang X, Han P, Tu Y, Ye S (2022c) Nanosheets-MnxOy anchored biochar for efficient removal of methyl blue and tetracycline from water. Chem Eng Res Des 182:13–24. https://doi.org/10.1016/j.cherd.2022.03.032

Lian J, Zhou F, Chen B, Yang M, Wang S, Liu Z, Niu S (2020) Enhanced adsorption of molybdenum(VI) onto drinking water treatment residues modified by thermal treatment and acid activation. J Clean Prod 244:118719. https://doi.org/10.1016/j.jclepro.2019.118719

Liang J, Li X, Yu Z, Zeng G, Luo Y, Jiang L, Yang Z, Qian Y, Wu H (2017) Amorphous MnO2 Modified Biochar Derived from Aerobically Composted Swine Manure for Adsorption of Pb(II) and Cd(II). ACS Sustainable Chem Eng 5:5049–5058. https://doi.org/10.1021/acssuschemeng.7b00434

Liao Q, Rong H, Zhao M, Luo H, Chu Z, Wang R (2022) Strong adsorption properties and mechanism of action with regard to tetracycline adsorption of double-network polyvinyl alcohol-copper alginate gel beads. J Hazard Mater 422:126863. https://doi.org/10.1016/j.jhazmat.2021.126863

Liu H, Xu G, Li G (2020) The characteristics of pharmaceutical sludge-derived biochar and its application for the adsorption of tetracycline. Sci Total Environ 747:141492. https://doi.org/10.1016/j.scitotenv.2020.141492

Liu X, Guo X, Liu Y, Lu S, Xi B, Zhang J, Wang Z, Bi B (2019) A review on removing antibiotics and antibiotic resistance genes from wastewater by constructed wetlands: Performance and microbial response. Environ Pollut 254:112996. https://doi.org/10.1016/j.envpol.2019.112996

Ma Y, Lu T, Tang J, Li P, Mašek O, Yang L, Wu L, He L, Ding Y, Gao F, Qi X, Zhang Z (2022) One-pot hydrothermal synthesis of magnetic N-doped sludge biochar for efficient removal of tetracycline from various environmental waters. Sep Purif Technol 297:121426. https://doi.org/10.1016/j.seppur.2022.121426

Ma Y, Qi Y, Yang L, Wu L, Li P, Gao F, Qi X, Zhang Z (2021) Adsorptive removal of imidacloprid by potassium hydroxide activated magnetic sugarcane bagasse biochar: Adsorption efficiency, mechanism and regeneration. J Clean Prod 292:126005. https://doi.org/10.1016/j.jclepro.2021.126005

Mei Y, Xu J, Zhang Y, Li B, Fan S, Xu H (2021) Effect of Fe-N modification on the properties of biochars and their adsorption behavior on tetracycline removal from aqueous solution. Bioresource Technol 325:124732. https://doi.org/10.1016/j.biortech.2021.124732

Ndagijimana P, Liu X, Xu Q, Li Z, Pan B, Liao X, Wang Y (2022) Nanoscale zero-valent iron/silver@activated carbon-reduced graphene oxide: Efficient removal of trihalomethanes from drinking water. Sci Total Environ 839:156228. https://doi.org/10.1016/j.scitotenv.2022.156228

Oladipo AA, Ifebajo AO (2018) Highly efficient magnetic chicken bone biochar for removal of tetracycline and fluorescent dye from wastewater: Two-stage adsorber analysis. J Environ Manage 209:9–16. https://doi.org/10.1016/j.jenvman.2017.12.030

Omidi MH, Azqhandi MHA, Ghalami-Choobar B (2022) Synthesis, characterization, and application of graphene oxide/layered double hydroxide /poly acrylic acid nanocomposite (LDH-rGO-PAA NC) for tetracycline removal: A comprehensive chemometric study. Chemosphere 308:136007. https://doi.org/10.1016/j.chemosphere.2022.136007

Pi Z, Li X, Wang D, Xu Q, Tao Z, Huang X, Yao F, Wu Y, He L, Yang Q (2019) Persulfate activation by oxidation biochar supported magnetite particles for tetracycline removal: Performance and degradation pathway. J Clean Prod 235:1103–1115. https://doi.org/10.1016/j.jclepro.2019.07.037

Raj V, Chauhan MS, Pal SL (2022) Potential of sugarcane bagasse in remediation of heavy metals: A review. Chemosphere 307:135825. https://doi.org/10.1016/j.chemosphere.2022.135825

Shaheen SM, Mosa A, Natasha Abdelrahman H, Niazi NK, Antoniadis V, Shahid M, Song H, Kwon EE, Rinklebe J (2022) Removal of toxic elements from aqueous environments using nano zero-valent iron- and iron oxide-modified biochar: a review. Biochar 4:24. https://doi.org/10.1007/s42773-022-00149-y

Shi W, Ren H, Li M, Shu K, Xu Y, Yan C, Tang Y (2020) Tetracycline removal from aqueous solution by visible-light-driven photocatalytic degradation with low cost red mud wastes. Chem Eng J 382:122876. https://doi.org/10.1016/j.cej.2019.122876

Singh M, Ahsan M, Pandey V, Singh A, Mishra D, Tiwari N, Singh P, Karak T, Khare P (2022) Comparative assessment for removal of anionic dye from water by different waste-derived biochar vis a vis reusability of generated sludge. Biochar 4:13. https://doi.org/10.1007/s42773-022-00140-7

Song W, Wu Z, Xu X, Wu H, Yao Y (2022) Nitrogen-doped carbon nanosheets with Fe-based nanoparticles for highly efficient degradation of antibiotics and sulfate ion enhancement effect. Chemosphere 294:133704. https://doi.org/10.1016/j.chemosphere.2022.133704

Song X, Shui B, Wang Y, Zhou J, Wang S, Wu N (2022b) Adsorption performance of GO-doped activated ATP composites towards tetracycline. RSC Adv 12:19917–19928. https://doi.org/10.1039/d2ra03023c

Song YX, Chen S, You N, Fan HT, Sun LN (2020) Nanocomposites of zero-valent Iron@Activated carbon derived from corn stalk for adsorptive removal of tetracycline antibiotics. Chemosphere 255:126917. https://doi.org/10.1016/j.chemosphere.2020.126917

Sun L, Li J, Li X, Liu C, Wang H, Huo P, Yan YS (2019) Molecularly imprinted Ag/Ag(3)VO(4)/g-C(3)N(4) Z-scheme photocatalysts for enhanced preferential removal of tetracycline. J Colloid Interf Sci 552:271–286. https://doi.org/10.1016/j.jcis.2019.05.060

Sun S, Jiang Q, Zhang W, Tian L, Li T, Zheng L, Gao Y, Zeng X, Zhou L (2022) Efficient adsorption of tetracycline in aquatic system by thermally-treated sediment. Environ Res 214:113779. https://doi.org/10.1016/j.envres.2022.113779

Tang J, Ma Y, Cui S, Ding Y, Zhu J, Chen X, Zhang Z (2022) Insights on ball milling enhanced iron magnesium layered double oxides bagasse biochar composite for ciprofloxacin adsorptive removal from water. Bioresource Technol 359:127468. https://doi.org/10.1016/j.biortech.2022.127468

Wang W, Gao M, Cao M, Dan J, Yang H (2021) Self-propagating synthesis of Zn-loaded biochar for tetracycline elimination. Sci Total Environ 759:143542. https://doi.org/10.1016/j.scitotenv.2020.143542

Wang W, Gao M, Cao M, Liu X, Yang H, Li Y (2021) A series of novel carbohydrate-based carbon adsorbents were synthesized by self-propagating combustion for tetracycline removal. Bioresource Technol 332:125059. https://doi.org/10.1016/j.biortech.2021.125059

Wang W, Kang R, Yin Y, Tu S, Ye L (2022) Two-step pyrolysis biochar derived from agro-waste for antibiotics removal: Mechanisms and stability. Chemosphere 292:133454. https://doi.org/10.1016/j.chemosphere.2021.133454

Wei J, Liu Y, Li J, Zhu Y, Yu H, Peng Y (2019) Adsorption and co-adsorption of tetracycline and doxycycline by one-step synthesized iron loaded sludge biochar. Chemosphere 236:124254. https://doi.org/10.1016/j.chemosphere.2019.06.224

Wei M, Marrakchi F, Yuan C, Cheng X, Jiang D, Zafar FF, Fu Y, Wang S (2022) Adsorption modeling, thermodynamics, and DFT simulation of tetracycline onto mesoporous and high-surface-area NaOH-activated macroalgae carbon. J Hazard Mater 425:127887. https://doi.org/10.1016/j.jhazmat.2021.127887

Wen J, Fu W, Ding S, Zhang Y, Wang W (2022) Pyrogallic acid modified nanoscale zero-valent iron efficiently removed Cr(VI) by improving adsorption and electron selectivity. Chem Eng J 443:136510. https://doi.org/10.1016/j.cej.2022.136510

Wu J, Hou B, Wang X, Liu Z, Wang Z, Liu B, Li S, Gao H, Zhu X, Mao Y (2022) Preparation of N, S-codoped magnetic bagasse biochar and adsorption characteristics for tetracycline. RSC Adv 12:11786–11795. https://doi.org/10.1039/d1ra08404f

Wu T, Xue Q, Liu F, Zhang J, Zhou C, Cao J, Chen H (2019) Mechanistic insight into interactions between tetracycline and two iron oxide minerals with different crystal structures. Chem Eng J 366:577–586. https://doi.org/10.1016/j.cej.2019.02.128

Xia Y, Luo H, Li D, Chen Z, Yang S, Liu Z, Yang T, Gai C (2020) Efficient immobilization of toxic heavy metals in multi-contaminated agricultural soils by amino-functionalized hydrochar: Performance, plant responses and immobilization mechanisms. Environ Pollut 261:114217. https://doi.org/10.1016/j.envpol.2020.114217

Xiang W, Zhang X, Luo J, Li Y, Guo T, Gao B (2022) Performance of lignin impregnated biochar on tetracycline hydrochloride adsorption: Governing factors and mechanisms. Environ Res 215:114339. https://doi.org/10.1016/j.envres.2022.114339

Xu D, Gao Y, Lin Z, Gao W, Zhang H, Karnowo K, Hu X, Sun H, Syed-Hassan SSA, Zhang S (2019) Application of Biochar Derived From Pyrolysis of Waste Fiberboard on Tetracycline Adsorption in Aqueous Solution. Front Chem 7:943. https://doi.org/10.3389/fchem.2019.00943

Xu J, Zhang Y, Li B, Fan S, Xu H, Guan DX (2022) Improved adsorption properties of tetracycline on KOH/KMnO$_4$ modified biochar derived from wheat straw. Chemosphere 296:133981. https://doi.org/10.1016/j.chemosphere.2022.133981

Xue Y, Guo Y, Zhang X, Kamali MM, Aminabhavi T, Appels L, Dewil R (2022) Efficient adsorptive removal of ciprofloxacin and carbamazepine using modified pinewood biochar – A kinetic, mechanistic study. Chem Eng J 450:137896. https://doi.org/10.1016/j.cej.2022.137896

Yang Q, Wu P, Liu J, Rehman S, Ahmed Z, Ruan B, Zhu N (2020) Batch interaction of emerging tetracycline contaminant with novel phosphoric acid activated corn straw porous carbon: Adsorption rate and nature of mechanism. Environ Res 181:108899. https://doi.org/10.1016/j.envres.2019.108899

Yang S, Liu Y, Shen C, Li F, Yang B, Huang M, Yang M, Wang Z, Sand W (2020) Rapid decontamination of tetracycline hydrolysis product using electrochemical CNT filter: Mechanism, impacting factors and pathways. Chemosphere 244:125525. https://doi.org/10.1016/j.chemosphere.2019.125525

Yu H, Gu L, Chen L, Wen H, Zhang D, Tao H (2020) Activation of grapefruit derived biochar by its peel extracts and its performance for tetracycline removal. Bioresource Technol 316:123971. https://doi.org/10.1016/j.biortech.2020.123971

Yuan M, Li C, Zhang B, Wang J, Zhu J, Ji J, Ma Y (2021) A mild and one-pot method to activate lignin-derived biomass by using boric acid for aqueous tetracycline antibiotics removal in water. Chemosphere 280:130877. https://doi.org/10.1016/j.chemosphere.2021.130877

Zeng S, Choi YK, Kan E (2021) Iron-activated bermudagrass-derived biochar for adsorption of aqueous sulfamethoxazole: Effects of iron impregnation ratio on biochar properties, adsorption, and regeneration. Sci Total Environ 750:141691. https://doi.org/10.1016/j.scitotenv.2020.141691

Zeng S, Kan E (2022) Sustainable use of $Ca(OH)_2$ modified biochar for phosphorus recovery and tetracycline removal from water. Sci Total Environ 839:156159. https://doi.org/10.1016/j.scitotenv.2022.156159

Zhang B, Liu J, Zhao RS, Xian Q (2021) NDMA adsorption and degradation by a new-type of Ag-MONT material carrying nanoscale zero-valent iron. Chemosphere 268:129271. https://doi.org/10.1016/j.chemosphere.2020.129271

Zhang G, Li L, Zhou G, Lin Z, Wang J, Wang G, Ling F, Liu T (2022) Recyclable aminophenylboronic acid modified bacterial cellulose microspheres for tetracycline removal: Kinetic, equilibrium and adsorption performance studies for hoggery sewer. Environ Pollut 307:119544. https://doi.org/10.1016/j.envpol.2022.119544

Zhang H, Song X, Zhang J, Liu Y, Zhao H, Hu J, Zhao J (2022) Performance and mechanism of sycamore flock based biochar in removing oxytetracycline hydrochloride. Bioresource Technol 350:126884. https://doi.org/10.1016/j.biortech.2022.126884

Zhang L, Dong Y, Liu J, Liu W, Lu Y, Lin H (2022) Promotion of higher synthesis temperature for higher-efficient removal of antimonite and antimonate in aqueous solution by iron-loaded porous biochar. Bioresource Technol 363:127889. https://doi.org/10.1016/j.biortech.2022.127889

Zhao Z, Nie T, Zhou W (2019) Enhanced biochar stabilities and adsorption properties for tetracycline by synthesizing silica-composited biochar. Environ Pollut 254:113015. https://doi.org/10.1016/j.envpol.2019.113015

Zheng Z, Zhao B, Guo Y, Guo Y, Pak T, Li G (2021) Preparation of mesoporous batatas biochar via soft-template method for high efficiency removal of tetracycline. Sci Total Environ 787:147397. https://doi.org/10.1016/j.scitotenv.2021.147397

Zhou Y, Liu X, Xiang Y, Wang P, Zhang J, Zhang F, Wei J, Luo L, Lei M, Tang L (2017) Modification of biochar derived from sawdust and its application in removal of tetracycline and copper from aqueous solution: Adsorption mechanism and modelling. Bioresource Technol 245:266–273. https://doi.org/10.1016/j.biortech.2017.08.178

Zhu J, Ma Y, Chen X, Tang J, Yang L, Zhang Z (2022) One-pot hydrothermal synthesis of MoS_2 modified sludge biochar for efficient removal of tetracycline from water. J Water Process Eng 49:103089. https://doi.org/10.1016/j.jwpe.2022.103089

Publisher's note Springer Nature remains neutral with regard to jurisdictional claims in published maps and institutional affiliations.

Springer Nature or its licensor (e.g. a society or other partner) holds exclusive rights to this article under a publishing agreement with the author(s) or other rightsholder(s); author self-archiving of the accepted manuscript version of this article is solely governed by the terms of such publishing agreement and applicable law.